Composites Part C: Open Access 18 (2025) 100640

Contents lists available at ScienceDirect

Composites Part C: Open Access

journal homepage: www.sciencedirect.com/journal/composites-part-c-open-access

Machining-induced burr distribution along hole contours in unidirectional carbon fibre-reinforced polymer (UD-CFRP) composites

Norbert Geier *, Gergely Magyar

Department of Manufacturing Science and Engineering, Faculty of Mechanical Engineering, Budapest University of Technology and Economics, Műegyetem rkp. 3., H-1111 Budapest, Hungary

ARTICLE INFO

Keywords:
Machining
Burr
Composite
CFRP
Digital image processing

ABSTRACT

Machining-induced burr formation in carbon fibre-reinforced polymer (CFRP) composites is difficult to predict and control, mainly due to the anisotropy and inhomogeneity of the fibrous composite, as well as the rapid tool condition change due to the abrasive tool wear. The main aim of this study is to develop a model to determine the density and distribution functions of risky fibre cutting angles where machining-induced burrs are expected to be formed when hole-machining CFRPs. Four models were introduced, and their adequacy was analysed. The coefficients of the models were determined using datasets of three previous research projects (*i.e.,* 2 380 808 data points) and validated through a fourth one (208 571 data points) where hole machining experiments were carried out using different tools, parameters and setups. The normality of the risky fibre cutting angles was tested through the Shapiro-Wilk and Kolmogorov-Smirnov statistical tests, and the distribution was found to be not Gaussian. The developed trigonometric model shows a good fit to the data points, *i.e.,* the determination coefficient is at least 0.949 for each dataset. The results indicate that machining-induced burr formation is most probable at a fibre cutting angle of 118–133°, and 60 % of burr occurrences fall within the 110°–160° range when the critical fibre cutting angle is 133° These findings provide a foundation for the industrial adoption of advanced machining strategies for fibrous polymer composites, enabling a significant reduction of machining-induced burrs in CFRPs.

1. Introduction

The application of carbon fibre reinforced polymer (CFRP) composite products is decisive and will further spread in high-tech applications such as structural elements of aeroplanes, wind-blades, automobiles, military and space vehicles, mainly due to their excellent specific strength and easy-to-shape [1]. Although these CFRP parts are often manufactured close to their final geometrical shape using advanced composite manufacturing technologies [2,3], mechanical machining is often needed to meet the required strict geometrical tolerances [4] and produce holes for assembly [5]. Machining of CFRPs is challenging because the anisotropy and inhomogeneity of the composite cause difficult-to-control chip removal [6], and the significant abrasive wear effect of the carbon reinforcing fibres rapidly changes the cutting tool condition [7–9]. Improper technology and rapidly changing tool conditions often result in machining-induced defects like burrs and delamination, which often result in the reduction of the resultant strength of the machined composite [10]. Thousands of holes are often needed in the industries for assembling CFRP parts using rivets or bolts [11]; thus, the appropriate planning of the machining technology of these holes is the focus of the industrial and scientific community.

This paper focuses on the machining-induced burr formation along the outer edges of holes machined in CFRP composites. According to Aurich et al. [12], machining-induced burr forms mainly due to the inappropriate mechanical support of the material; thus, burr formation is expected only on the outer edges of homogeneous materials. In the case of composites, burr may form interlayer also [13–15]. Nevertheless, if the carbon fibres are totally embedded in the matrix with an excellent adhesion quality (*i.e.* no voids and material discontinuity arise), burr is expected to be formed only on the edges of CFRP composites rather than in the interlayer. Although the burr formation in metals is governed by plastic deformation, the burr formation in CFRPs is governed mostly by unsupported out-of-plane fibre deflection and macroscopic fibre fracture [16–18]. Ahmad [6] summarised the categorical chip removal modes of fibrous polymers and highlighted that the fibre cutting angle (*i.e.* the angle between the cutting speed and fibre direction) primarily affects it. Therefore, researchers are attempting to find a relationship between the

* Corresponding author.
E-mail address: geier.norbert@gpk.bme.hu (N. Geier).

https://doi.org/10.1016/j.jcomc.2025.100640

Available online 19 August 2025

Nomenclature

a_i	regression coefficients
b_i	regression coefficients
c_i	regression coefficients
C_k	centre point of the nominal hole contour
e_k	equation of the nominal hole contour
e_f	equation of the contour of the drilled hole
f	density function
F	distribution function
H	error function
k	fibre direction
L_θ	list of burred contour points
M	median
P	probability
P_i	projects
r	radius of the nominal hole contour
S_p	burr function
u	horizontal coordinate of the C_k
v	vertical coordinate of the C_k
v_c	cutting speed
α	significance level
δ	extend of burr zone
Δ	hole radius offset
θ	fibre cutting angle
θ’	transformed fibre cutting angle
θ_c	critical fibre cutting angle
μ	expected value
σ	deviation
φ	angular running parameter

fibre cutting angle and burr occurrence.

Su et al. [19] and Jaiswal and Park [20] analytically investigated burr formation by modelling fibres in unsupported composite layers as cantilever beams, employing a Winkler elastic foundation and Euler–Bernoulli beam theory, respectively. Their analyses identified the fibre cutting angle as the dominant parameter influencing burr formation, while showing a relatively weak sensitivity to cutting force [21]. However, simplifying the complex burr formation mechanism in CFRP drilling to a cantilever beam neglects critical matrix–fibre interactions and the associated energy dissipation mechanisms. To address these limitations, researchers have developed microscopic numerical models that explicitly represent fibres, matrix, and their interfaces, incorporating advanced damage criteria (*e.g.*, three-dimensional Hashin), realistic frictional contact conditions, and thermo-mechanical coupling effects [22]. For example, Bi et al. [23] reported a numerical prediction error of only ~12.7 % for the burr factor at the drilling exit using such an advanced multiscale finite element model. While these numerical approaches provide valuable insights into the multi-physics nature of burr formation and are expected to drive future predictive capabilities, their computational cost remains high, particularly for fully microscopic simulations in which individual fibres, the surrounding matrix, and cohesive zones are explicitly modelled.

Based on other researchers’ [24–27] and own experimental experiences [18,28–31], the machining-induced burr formed during machining holes in unidirectional carbon fibre reinforced polymer (UD-CFRP) composites forms in the range of (θ_c–δ_1°; θ_c+δ_2°), mainly due to the local bending-dominant chip formation mechanism and significant fibre deflections due to the lack of mechanical support [32]. Xu et al. [25] reported that the machining-induced burr formed along the hole contour can usually be observed in two burr areas, as shown in Fig. 1, typically with an expected value (*i.e.* critical fibre cutting angle) along the nominal contour of θ_c≈135° [32].

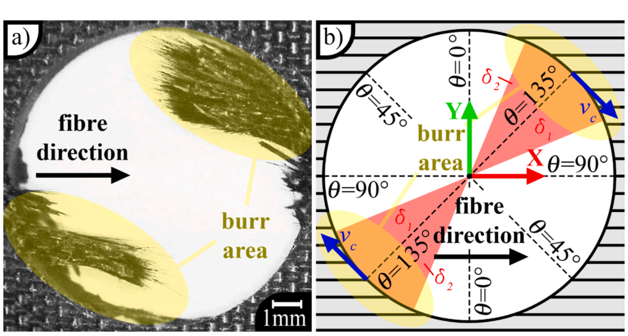

Fig. 1. Symmetrically located burr areas along the entrance edge contour of a hole machined in a polymer composite reinforced with unidirectional carbon fibres [33]: a) unprocessed image where the area highlighted in yellow is the burr area, b) schematic illustration where the red area corresponds to the risky fibre cutting angle range.

Hrechuk et al. [24] analysed the quality of drilled holes in UD-CFRP. They proposed a novel inspection technique based on digital image processing and related measure generation methods inspired by the surface roughness measures. They observed that the burr is typically formed in the two burr areas and increases significantly with the increase of tool wear. Xu et al. [26] drilled holes in CFRP composites using brad and spur, twist and dagger drills and analysed the hole quality. They reported that the tool geometry and the feed have significant influences on the amount of machining-induced burr. Furthermore, it can be seen from their figures on the holes that the more the burr, the better recognisable the burr areas, because if only a few fibres are uncut, the burr areas are difficult to statistically identify. Xu et al. [25] observed during CFRP drilling that the machining-induced burr area is significantly influenced by the feed; however, the critical fibre cutting angle seems not to be influenced by either the feed or the tool wear. Although Lissek et al. [34] focused on quantifying and analysing the drilling-induced delamination in their study, their images show that the longest drilling-induced burr is located close to the widest delaminated area, *i.e.* these damages are formed at a critical fibre cutting angle of 135°, approximately.

Collectively, these factors—composite anisotropy and inhomogeneity; insufficient mechanical support at machined edges; the dominant role of fibre cutting angle; sensitivity to tool wear; and the absence of standardised inspection methods—render burr formation in CFRP machining a highly localised and complex phenomenon. As a result, no universally applicable predictive model or evaluation protocol currently exists, highlighting the need for robust criteria and standardised measurement techniques. To address this gap, the present study develops a quantitative model for identifying those fibre cutting angles that are most critical to burr formation in CFRP composites. We performed, therefore, hole machining experiments in various UD-CFRP composites to (i) examine the expected critical location (θ_c) and related extent (δ_i) of the burr zone according to the setup presented in Section 2; and (ii) developed models for the density and distribution of risky fibre cutting angle for the support of machining technology planning of unidirectional and non-unidirectional fibrous polymeric composites, as presented in Section 3.

2. Materials and methods

In order to determine the circumferential distribution and critical range of the machining-induced burr formed along the contour of holes produced by machining unidirectional carbon fibre reinforced polymer (UD-CFRP) composite plates, we used our historical data (digital images), which were not processed in a similar way previously. The digital images were taken within the framework of the projects listed below (P_1-P_3).

- P_1: development of a process monitoring and diagnostic method for the production of high-quality holes by helical milling in UD-CFRP composites [28,29].
- P_2: energetic characterisation of the quality of the holes machined into the side of the UD-CFRP composite plate and the drilling technology [18].
- P_3: comparative study of hole machining technologies in UD-CFRP composite [30].

In the P_1 project [28,29], holes with a nominal diameter of 10 mm were machined into a unidirectional carbon fibre-reinforced vinyl ester matrix composite plate having a nominal thickness of 6 mm. The holes were produced by helical milling with an 8 mm diameter, single-edged, uncoated Tivoly 80308810808 type HSS helical end mill (Fig. 2d). A total of 111 holes were machined with a feed of 0.06 mm and a cutting speed of 150 m/min, with variable pitch and depth, without the use of cooling and lubricating fluid in the experimental setup shown in Fig. 2a. Axial images of the holes were taken with a Dino-Lite AM4013MT type digital microscope (10x nominal magnification and 1280 × 1024 pixels resolution).

In the P_2 project [18], we drilled 13 through holes with a nominal diameter of 11.2 mm in unidirectional carbon fibre-reinforced epoxy resin matrix (FM20 resin and MH3124 crosslinker in a ratio of 100:35) polymer composite. We machined the holes with an 11.2 mm diameter TIVOLY 11400111120 type (Fig. 2e), uncoated twist drill, under dry working conditions in the experimental setup shown in Fig. 2b The cutting speed and the feed rate were varied between 50–150 m/min and 70–300 mm/min, respectively, at five levels based on the Central Composite Inscribed (CCI) experimental design, with four repetitions of the base point. We took pictures of the holes from the axial direction with a Dino-Lite AM4013MT type digital microscope (10x nominal magnification and 1280 × 1024 pixels resolution).

In the P_3 project [30], holes with a nominal diameter of 12 mm were machined into a unidirectional carbon fibre-reinforced vinyl ester matrix composite plate having a nominal thickness of 6 mm in the experimental setup shown in Fig. 2c. The holes were produced with pre-drilling (pilot hole drilling) and then hole-enlarging (round milling) operation elements. The pilot hole drilling operations were carried out with an 11.138 mm diameter double-point Seco SD205A-11.138-53-12R1-C1 type diamond-coated drill (Fig. 2f) and an 8 mm diameter DIN338 standard Tivoly 11451010800 HSS twist drill (Fig. 2g). We used 4-, 6- and 8- mm diameter single-edged Tivoly VHM ALU type (82329710400, 82329710600, 82329710800) uncoated carbide end mills for the milling operations (Fig. 2h). The diameter of the milling tool (4, 6, 8 mm) and the feed (0.01, 0.04, 0.07 mm) were varied based on the full factorial experimental design. Each operation element was realised in dry machining conditions, as well as the circular milling operation elements with down milling. Axial images of all drilled pilot holes and final enlarged holes (52 samples in total) were acquired using a Dino-Lite AD7013MZT digital microscope, operating at a nominal magnification of 10 × with a resolution of 1280 × 1024 pixels.

We processed the digital images taken during the P_1- P_3 projects with the algorithm realised in the main points below.

(i) Import the input images into a Python program using image processing and basic mathematical tools.
(ii) Converting the images to grayscale by linearly combining the three basic colours (red, green, blue) based on Eq. (1).

$$\boldsymbol{C} = \begin{pmatrix} c_{11} & \cdots & c_{1m} \\ \vdots & \ddots & \vdots \\ c_{n1} & \cdots & c_{nm} \end{pmatrix}, \; c_{ij} = 0.3\cdot\boldsymbol{R} + 0.59\cdot\boldsymbol{G} + 0.11\cdot\boldsymbol{B} \qquad (1)$$
$$i = 1\ldots n; j = 1\ldots m, \; c_{ij} \in \{0\ldots255\}$$

Where $\boldsymbol{R} \in \{0\ldots255\}$, $\boldsymbol{G} \in \{0\ldots255\}$, and $\boldsymbol{B} \in \{0\ldots255\}$ denoting the red, green and blue layers of the input images, respectively.

(iii) Intensity-based segmentation of grayscale image pixels with a threshold calculated using the Otsu method [37] into white (1) and black (0) pixels (representative images are shown in Fig. 3).
(iv) Determining the e_k: $(x-u)^2+(y-v)^2 = r^2$ equation of the circle with centre of $C_k(u;v)$ and radius of r describing the nominal hole contour by selecting the circle with the largest radius that can be inscribed (Fig. 4b) around the contour curve of e_f (Fig. 4a).
(v) determination of circles of e_{k+} and e_{k-}, which are concentric with the e_k circle, the radius of which circles are respectively $(0.95+\Delta)\cdot r$ and $(0.95 - \Delta)\cdot r$ mm, where $\Delta = 0.02$ (Fig. 4d).
(vi) Manual determination of k vectors specifying the nominal fibre direction in accordance with the setting documented in the related experimental protocol.
(vii) Assigning a fibre cutting angle of θ_φ to each contour point of the e_k circle, taking into account the fibre direction characterised by the

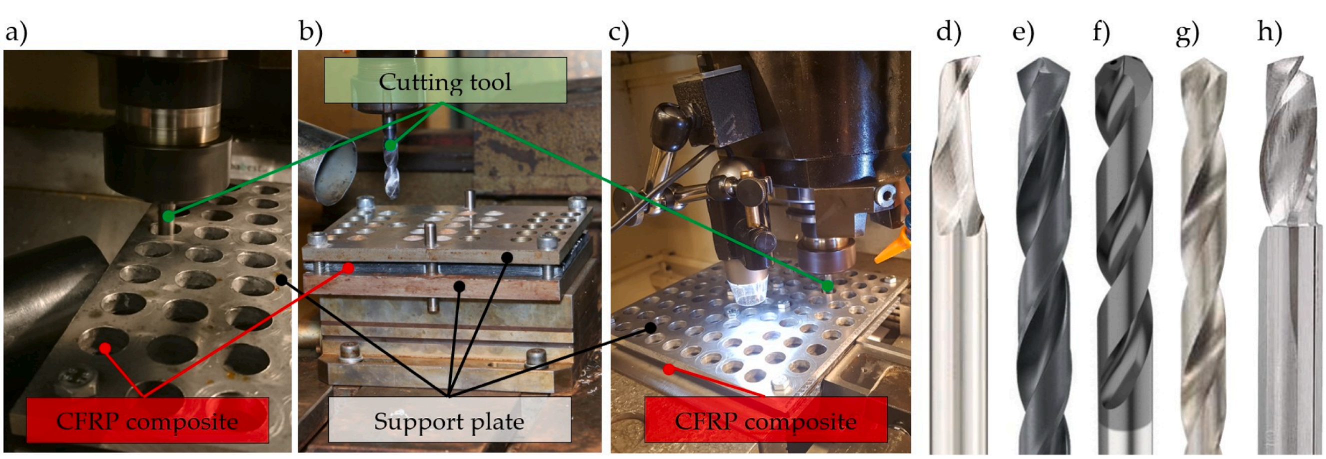

Fig. 2. Experimental setups for the a) P_1 [28,29], b) P_2 [18] and c) P_3 [30] projects, and the applied cutting tools: d) Tivoly 80308810808 helical end mill [35], e) TIVOLY 11400111120 uncoated twist drill [35], f) Seco SD205A-11.138-53-12R1-C1 double-point angle, diamond-coated twist drill [36], g) Tivoly DIN338 HSS twist drill [35], h) Tivoly VHM ALU uncoated solid-carbide end mill [35].

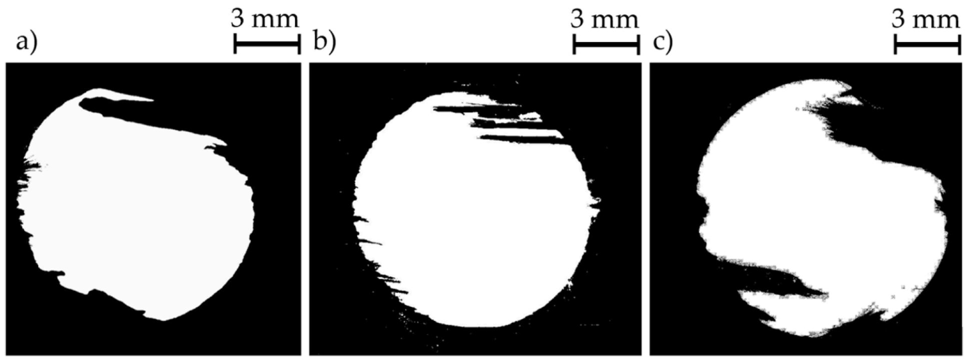

Fig. 3. Representative segmented images from the a) P_1, b) P_2 and c) P_3 projects.

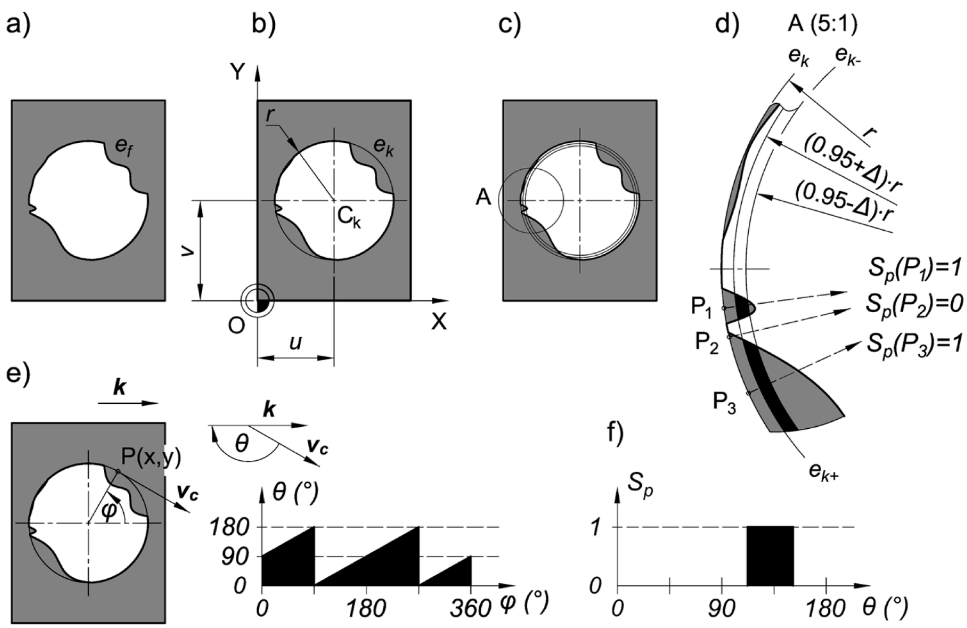

Fig. 4. Illustration of the algorithm for determining the circumferential distribution and critical range of the machining-induced burr: a) machined hole characterized by the contour e_f, b) e_k nominal hole contour, c)d) illustration of the burr area cut out by circles with the equations e_{k+} and e_{k-}, e) determination of fibre cutting angle (θ), f) incidence of machining-induced burr as a function of fibre cutting angle.

vector k and the cutting speed vector v_c assigned to the main edge of the tool (Fig. 4e).

(viii) determining the presence (1) or absence (0) of a machining-induced burr associated with each contour point of the e_k circle, such that the presence of a burr (1) of at least one black pixel on the section cut from radius r by the e_{k+} and e_{k-} circles.

(ix) Determination of the list of $S_p(\theta) = \{s_1 \ldots s_n\} \in (0;1)$ describing the machining-induced burr depending on the fibre cutting angle by matching the outputs of steps vii) and viii).

We plotted the radius of the circles fitted in step iv) of the algorithm in a dot diagram (Fig. 5a), so that anomalies not treated by the algorithm (additional information resulting from a shiny surface, continuity errors, *etc.*) can be filtered out. In the area framed in red on the dot diagram, circles with radii whose sizes differ significantly from those expected for each project have been fitted. Images characterised by these outliers were not included in the further processing.

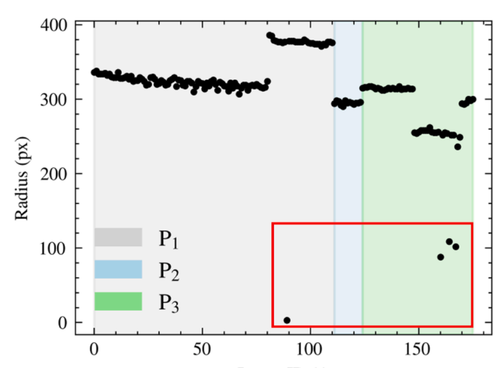

Fig. 5. Matching diagram of circles with centre of $C_k(u;v)$ and radius of r.

3. Results and discussion

3.1. Density of fibre cutting angle where machining-induced burrs formed

The lists of $S_p(\theta) = \{s_1 \ldots s_n\} \in (0;1)$ describing the machining-induced burr depending on the fibre cutting angle *(θ)* were summarized for each project (P_1, P_2, P_3) in order to minimize the effect of non-systematic errors (*e.g.* material error, clamping inaccuracy, image capturing inaccuracy). As a result of this summation, the number of $s_i = 1$ elements (*i.e.* pixels containing burrs) of projects P_{1-3} realised in $N_1 = 1\,720\,115$, $N_2 = 132\,060$ and $N_3 = 528\,633$ data elements, respectively. We put the fibre cutting angle values for these $s_i = 1$ data in a $L_\theta=\{\theta_1 \ldots \theta_N\}$ list for each project, and then, due to the nature and abundance of the data, we created histograms using a class width of 10° We interpreted these histograms as an estimate of the density of the fibre cutting angles in which burr formation is expected (*i.e.* risky fibre cutting angles). The histograms determined based on the data of the P_1- P_3 projects are shown in Fig. 6.

In order to use the density function of the normal (Gaussian) distribution to estimate the probability of a machining-induced burr occurring in a given fibre cutting angle range, we transformed the density functions in such a way that the middle element (median of *M*) of the ordered L_θ list is placed in the middle of the abscissa axis (Fig. 7). Technically, this transformation carries no risk due to the periodicity of the function *θ(φ)*, since the nominal probability of the formation of a machining-induced burr (*S*) is the same in all cases of $P(S_p)=k\cdot 180^\circ\cdot\theta$, where $k \in N$ and *P* denotes the probability. The *M* medians of the L_θ lists of projects P_{1-3} take the values of 114.59, 118.04 and 120.68, respectively. The fibre cutting angle is interpreted as the sum of the transformed fibre cutting angle (*θ'*) and the median (*M*) as expressed by Eq. (2).

$$\theta = \theta' + M \tag{2}$$

Due to the bell-shaped shape of the transformed histograms, we assumed that the fibre cutting angle – where machining-induced burr formed – follows a normal distribution (Gaussian distribution). Therefore, we checked the normality of the data series with the Shapiro-Wilk and Kolmogorov-Smirnov statistical tests (null hypothesis: the variable follows a normal distribution). We rejected the null hypothesis in the case of all three projects, since (i) the calculated p-values (see in Table 1) were all significantly lower than the selected $\alpha = 0.05$ significance level, and (ii) the normality curves (see in Fig. 8) clearly diverge significantly from the red normal line, so the distribution of fibre cutting angle cannot be considered to be Gaussian.

We searched for the estimate of the transformed density function of the risky fibre cutting angle in the general forms defined in Eqs. (3–6), where *f(θ')* denotes the estimate of the transformed density function of the list $L_\theta = \{\theta_1 \ldots \theta_N\}$, σ denotes the standard deviation, μ is the mean of the distribution, and a_i, b_i and c_i denote the regression coefficients of the third degree (pol3) and fourth degree (pol4) polynomial and the trigonometric (trig) equation, respectively.

$$f_{norm}(\theta') = \frac{1}{\sigma\sqrt{2\pi}} \cdot e^{-\frac{(\theta'-\mu)^2}{2\sigma^2}}, \text{ where} \qquad \sigma = \sqrt{\frac{1}{N}\sum_{i=1}^{N}\left(\theta'_i - \frac{1}{N}\sum_{i=1}^{N}\theta'_i\right)^2} \tag{3}$$

$$f_{pol3}(\theta') = a_1\cdot\theta'^3 + a_2\cdot\theta'^2 + a_3\cdot\theta' + a_4 \tag{4}$$

$$f_{pol4}(\theta') = b_1\cdot\theta'^4 + b_2\cdot\theta'^3 + b_3\cdot\theta'^2 + b_4\cdot\theta' + b_5 \tag{5}$$

$$f_{trig}(\theta') = c_1\cdot\sin(2\pi\cdot c_2\cdot\theta' + c_3) + c_4 \tag{6}$$

The values of the regression coefficients (a_i, b_i and c_i) were determined by numerical optimisation based on the method of least squares, including a maximum of 100,000 iteration steps. The regression coefficients of the density function *f(θ')* are summarised in Table 2, and the density functions are shown in Fig. 9.

The density functions fit the histograms with an accuracy characterised by the coefficients of determination (R^2) listed in Table 3. The fourth-order polynomial and trigonometric estimation gave the best determination coefficients between 0.937 and 0.991. The density function of the normal distribution is characterised by determination coefficients of 0.811–0.935. Considering that the trigonometric model showed a minimum fit of R^2=0.949 for all three projects, and the number of its regression coefficients is less than that of the fourth-order polynomial model, we selected the trigonometric approximation to estimate the density function of the cutting angle.

3.2. *Distribution of fibre cutting angle where machining-induced burrs formed*

The integral of the density function *f(θ')* according to Eq. (7) gives the *F(θ')* distribution function of the risky fibre cutting angle. Using the distribution function according to Eq. (8), the probability (*P*) of machining-induced burr formation can be estimated in a given range ($\theta'_c-\delta_1^\circ$; $\theta'_c+\delta_2^\circ$).

$$F(\theta') = \int_{-90}^{\theta} f(\theta')\, d\theta' \tag{7}$$

$$P(\theta'_c - \delta_1 \le \theta' \le \theta'_c + \delta_2) = F(\theta'_c + \delta_2) - F(\theta'_c - \delta_1) \tag{8}$$

We substituted the general form of the trigonometric density function into Eq. (7) and calculated the integral, giving the distribution function using the substitution integral method ($u = 2\pi\cdot c_2\cdot\theta'$), according to the main steps shown below.

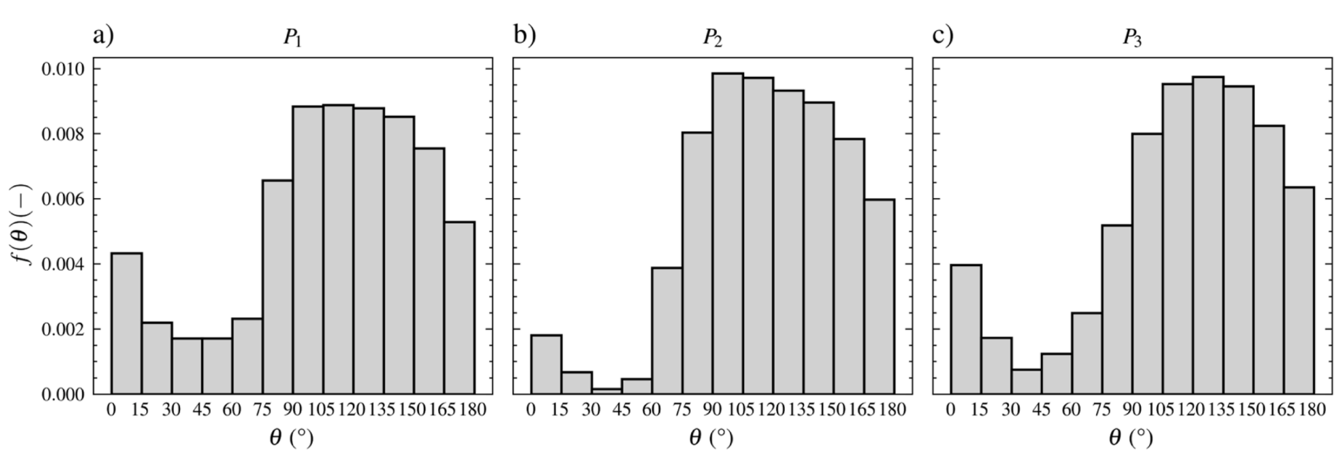

Fig. 6. Histograms determined based on data from a) P_1, b) P_2 and c) P_3 projects.

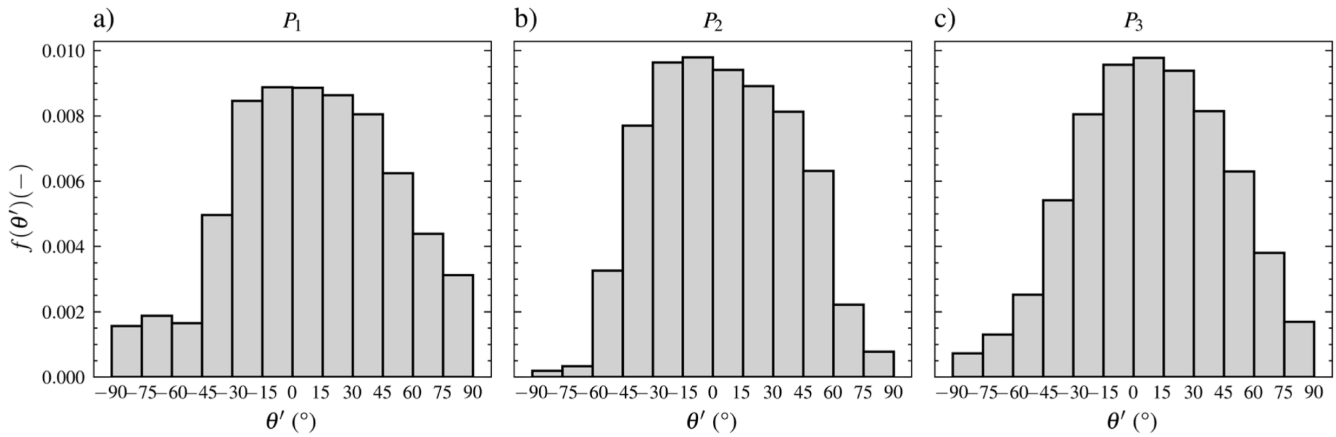

Fig. 7. Transformed histograms determined based on data from a) P_1, b) P_2 and c) P_3 projects.

Table 1
p-values for rejecting the null hypothesis of normality.

Project	p-values	
	Shapiro-Wilk	Kolmogorov-Smirnov
P_1	1.048E-19	0.000
P_2	8.110E-23	0.000
P_3	8.452E-15	0.000

$$F(\theta') = \int_{-90}^{\theta'} (c_1 \cdot \sin(2\pi \cdot c_2 \cdot \theta' + c_3) + c_4)\ d\theta' \tag{9}$$

$$F(\theta') = c_1 \cdot \underbrace{\int_{-90}^{\theta'} \sin(2\pi \cdot c_2 \cdot \theta' + c_3) d\theta'}_{A} + \underbrace{\int_{-90}^{\theta'} c_4 d\theta'}_{B} \tag{10}$$

$$u = 2\pi \cdot c_2 \cdot \theta' + c_3; du = 2\pi \cdot c_2 d\theta' \rightarrow \frac{du}{2\pi \cdot c_2} = d\theta' \tag{11}$$

$$A = c_1 \cdot \int_{-90}^{\theta'} \sin(u)\ \frac{du}{2\pi \cdot c_2} = \frac{c_1}{2\pi \cdot c_2} \int_{-90}^{\theta'} \sin(u)\ du = \frac{c_1}{2\pi \cdot c_2}(-\cos\ (u)) \tag{12}$$

$$A = \left[-\frac{c_1}{2\pi \cdot c_2} \cos\ (2\pi \cdot c_2 \cdot \theta' + c_3) \right]_{-90}^{\theta'} \tag{13}$$

$$F(\theta') = A + B = \left[-\frac{c_1}{2\pi \cdot c_2} \cos\ (2\pi \cdot c_2 \cdot \theta' + c_3) \right]_{-90}^{\theta'} + [c_4 \theta]_{-90}^{\theta'} \tag{14}$$

$$F(\theta') = \frac{c_1}{2\pi \cdot c_2} (\cos(- 180\pi \cdot c_2 + c_3) - \cos(2\pi \cdot c_2 \cdot \theta' + c_3)) + c_4(\theta' + 90) \tag{15}$$

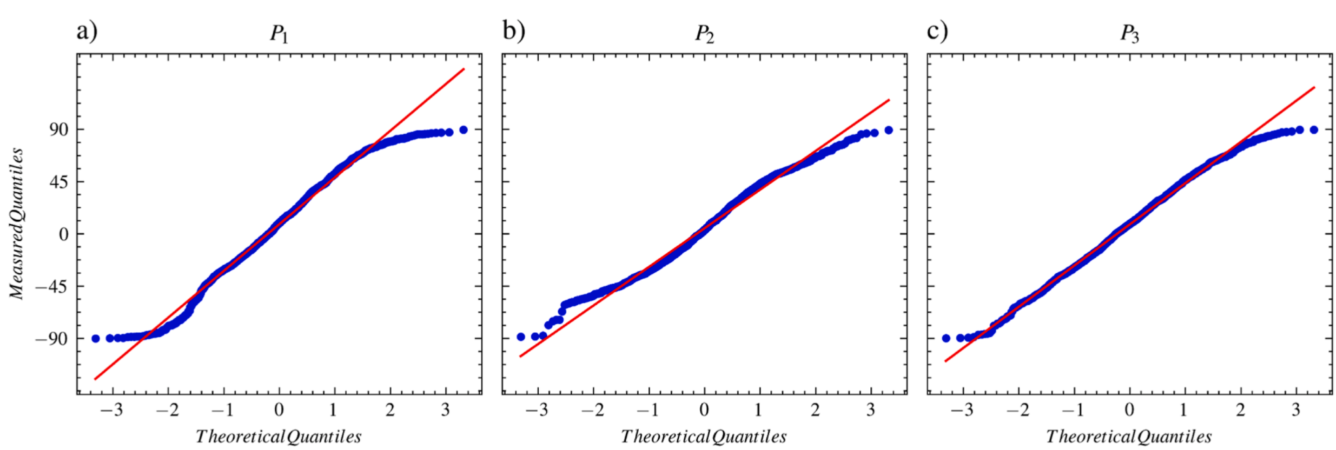

Fig. 8. Normality curves for testing the normal distribution of risky fibre cutting angles for projects a) P_1, b) P_2, and c) P_3.

Table 2
Regression coefficients of the density function $f(\theta')$.

Project	μ	σ	a_1	a_2	a_3	a_4	b_1	b_2
P_1	9.88E + 00	3.93E + 01	−5.19E-09	−1.09E-06	3.50E-05	8.47E-03	1.74E-10	−1.71E-09
P_2	5.00E + 00	3.34E + 01	−1.80E-09	−1.52E-06	4.01E-06	9.62E-03	1.48E-10	1.15E-09
P_3	8.71E + 00	3.62E + 01	−5.72E-09	−1.34E-06	3.26E-05	9.14E-03	1.65E-10	−2.43E-09
Project	b_3	b_4	b_5	c_1	c_2	c_3	c_4	
P_1	−2.25E-06	2.31E-05	9.39E-03	4.03E-03	5.34E-03	1.32E + 00	5.41E-03	
P_2	−2.51E-06	−6.02E-06	1.04E-02	5.97E-03	4.60E-03	−4.69E + 00	4.38E-03	
P_3	−2.45E-06	2.14E-05	1.00E-02	4.77E-03	5.32E-03	1.41E + 00	5.35E-03	

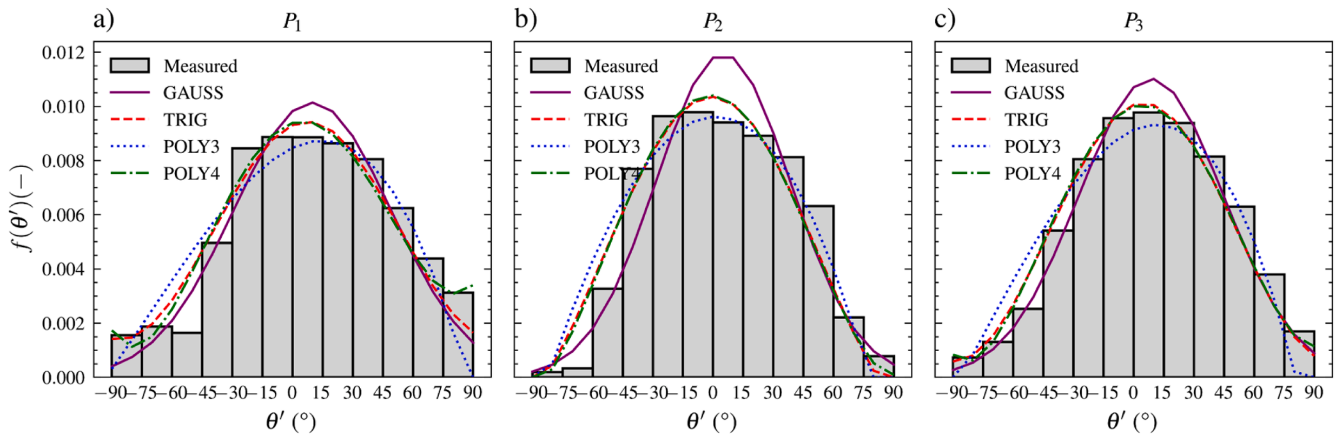

Fig. 9. Estimates of the density functions determined based on the data of the a) P_1, b) P_2, and c) P_3 projects.

Table 3
Coefficients of determination of $f(\theta)$ density functions.

Project	R^2			
	$f_{norm}(\theta')$	$f_{pol3}(\theta')$	$f_{pol4}(\theta')$	$f_{trig}(\theta')$
P_1	0.882	0.866	0.949	0.937
P_2	0.811	0.920	0.955	0.951
P_3	0.935	0.935	0.991	0.988

The $F(\theta')$ distribution functions of the fibre cutting angle calculated on the basis of projects P_{1-3} (regression coefficients $c_1 \ldots c_4$ substituted into Eq. (15)) are illustrated in Fig. 10. The coefficients of determination of the distribution functions are respectively 0.997, 0.997 and 0.999 for projects P_{1-3}. The $\overline{H}(\theta')$ average error function of the $F(\theta')$ distribution functions of the P_{1-3} data series characterised by the trigonometric density function was determined based on Eq. (16) and illustrated in Fig. 11.

$$\overline{H}(\theta') = \frac{1}{n}\sum_{i=1}^{n}\frac{|\overline{F}(\theta') - F_i(\theta')|}{F_i(\theta')}, \text{ where } \overline{F}(\theta') = \frac{1}{n}\sum_{i=1}^{n}F_i(\theta') \tag{16}$$

Based on the $\overline{H}(\theta')$ average error function illustrated in Fig. 11, it can be stated that (i) the maximum absolute relative error is 0.0298 (< 3 %) over the entire fibre cutting angle range, (ii) the error function is not monotonic and has several inflection points and (iii) the maximum value of the error is at a fibre cutting angle of $\theta' \approx 20°$ These error characteristics limit the use of the trigonometric approximation of the distribution function.

If we consider the M median of the list L_θ as the critical cutting angle, *i.e.* $\theta_c = M$, then the probability of $P(\theta'_c - \delta_1 \leq \theta \leq \theta'_c + \delta_2)$ falling in the vicinity of θ_c is given by the parametric equation below. The three-dimensional representations of Eq. (18) characterised by variables of δ_1 and δ_2 ($\delta_2 \neq \delta_1$) and regression coefficients of $c_1 \ldots c_4$ per project P_{1-3} can be seen in Fig. 12.

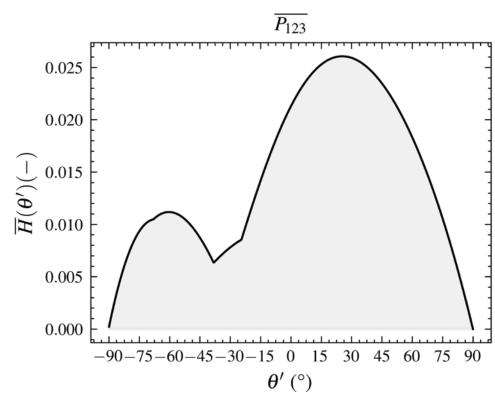

Fig. 11. The $\overline{H}(\theta')$ average error functionof the $F(\theta')$ distribution functions of the data series P_{1-3} characterized by the trigonometric density function.

$$P(\theta'_c - \delta_1 \leq \theta' \leq \theta'_c + \delta_2) = F(\theta'_c + \delta_2) - F(\theta'_c - \delta_1) := P_{\delta_{12}}(\theta') \tag{17}$$

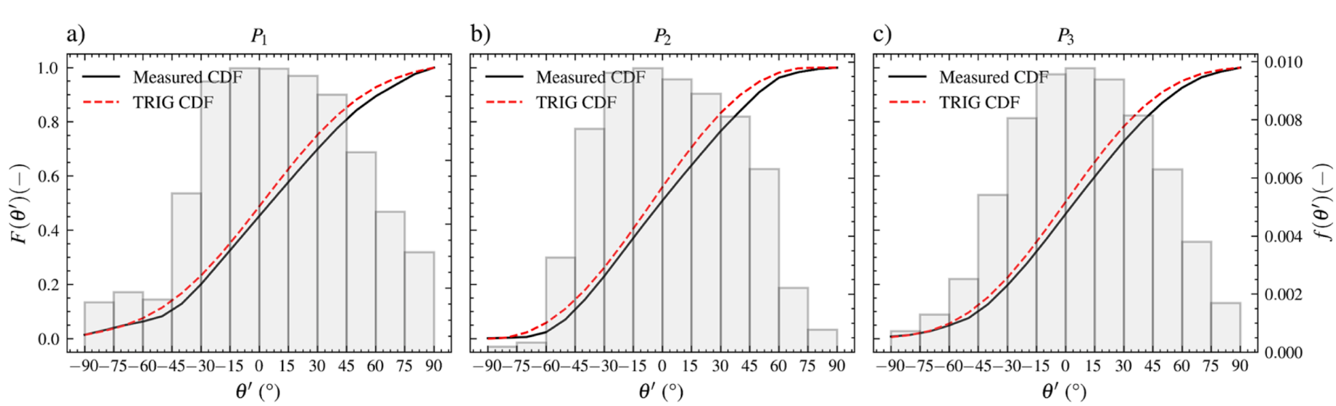

Fig. 10. Estimates of the distribution functions determined based on the data of the a) P_1, b) P_2, and c) P_3 projects.

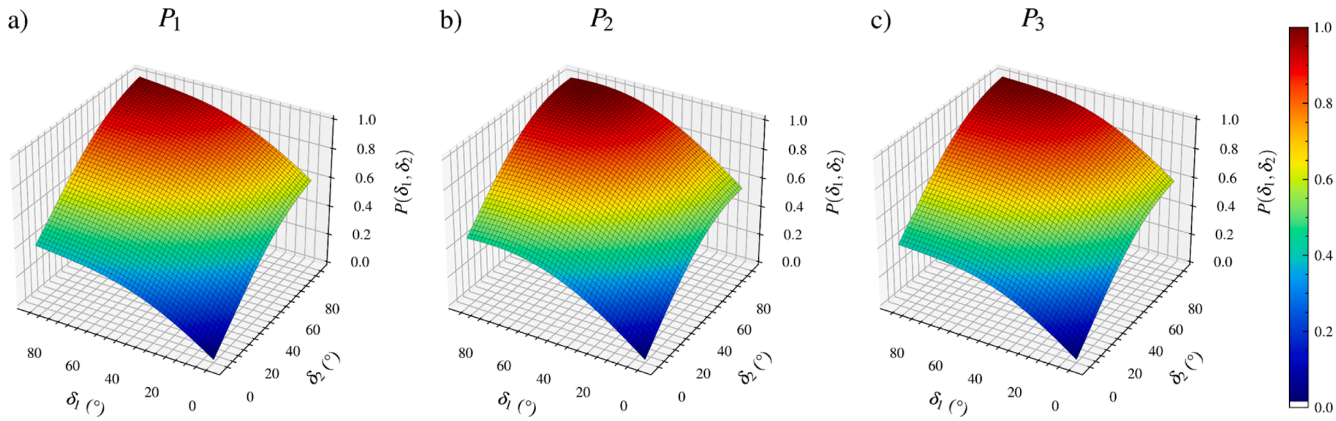

Fig. 12. Illustration of $P(\theta'_c - \delta_1 \leq \theta' \leq \theta'_c + \delta_2)$ probability functions determined based on the data of a) P_1, b) P_2 and c) P_3 projects.

$$P_{\delta_{12}}(\theta') = \frac{c_1}{2\pi \cdot c_2}(\cos(-180\pi \cdot c_2 + c_3) - \cos(2\pi \cdot c_2 \cdot (\theta'_c + \delta_2) + c_3)) + c_4((\theta'_c + \delta_2) + 90) - \frac{c_1}{2\pi \cdot c_2}(\cos(-180\pi \cdot c_2 + c_3) + \cos(2\pi \cdot c_2 \cdot (\theta'_c - \delta_1) + c_3)) - c_4((\theta'_c - \delta_1) + 90) \tag{18}$$

If the angle values of δ_1 and δ_2 measured from the critical fibre cutting angle of θ'_c are considered equal ($\delta_1 = \delta_2 := \delta$), Eq. (18) can be simplified according to Eq. (19). The parametric equation below gives the $P(\theta'_c - \delta \leq \theta \leq \theta'_c + \delta)$ probability of a machining-induced burr in the vicinity of the critical fibre cutting angle of $(\theta'_c - \delta; \theta'_c + \delta)$. The graphical representation of Eq. (20) can be seen in Fig. 13. Considering the quasi-symmetric environment of the maxima of the density functions, the simplification of $\delta_1 = \delta_2 := \delta$ is technologically justified.

$$P(\theta'_c - \delta \leq \theta' \leq \theta'_c + \delta) = F(\theta'_c + \delta) - F(\theta'_c - \delta) := P_\delta(\theta') \tag{19}$$

$$P_\delta(\theta') = \frac{c_1}{2\pi \cdot c_2}(\cos(-180\pi \cdot c_2 + c_3) - \cos(2\pi \cdot c_2 \cdot (\theta'_c + \delta) + c_3)) + c_4((\theta'_c + \delta) + 90) - \frac{c_1}{2\pi \cdot c_2}(\cos(-180\pi \cdot c_2 + c_3) - \cos(2\pi \cdot c_2 \cdot (\theta'_c - \delta) + c_3)) - c_4((\theta'_c - \delta) + 90) \tag{20}$$

3.3. Validation and discussion

We validated the applicability of the described trigonometric density functions and distribution functions with another set of experimental data. During the validation experiments, holes with a nominal diameter of 10 mm were machined into a unidirectional carbon fibre-reinforced vinyl ester matrix composite plate with a nominal thickness of 6 mm [31,38]. These holes were drilled with a 10 mm diameter Tivoly Polaris 150 Sim Dim 6537 K (82,415,011,000) TiAlN coated twist drill. The cutting speed (50; 100; 150 m/min) and the feed (0.05; 0.10; 0.15 mm) were varied in 3–3 levels according to the central composite face-centred (CCF) experimental design, in addition to repeating the basic point four times. We captured pictures of the holes with a Mitutoyo Quick Image QI-A505 type digital microscope (with 10x nominal magnification and 1280 × 960 pixel resolution). The average of the trigonometric density functions (calculated based on Eq. (21)) fitted to the transformed datasets of projects P_{1-3} fits the validation dataset with an accuracy characterized by a coefficient of determination of 0.834, while in the case of the distribution function (calculated based on Eq. (22)), the coefficient of determination is 0.977. Fig. 14 illustrates the goodness of the fits. The coefficients of determination suggest that the developed data collection method and related evaluation can be appropriately used to estimate the distribution of risky fibre cutting angles in UD-CFRP plates.

$$\overline{f(\theta')} = \frac{1}{n}\sum_{i=1}^{n=3} f_i(\theta') \tag{21}$$

$$\overline{F(\theta')} = \frac{1}{n}\sum_{i=1}^{n=3} F_i(\theta') \tag{22}$$

The described trigonometric models and related evaluation procedures, characterised by excellent coefficient of determinations, are suitable for determining the fibre cutting angle range in which there is a high probability of the formation of a machining-induced burr on the machined hole contours of UD-CFRP composites. Our estimated critical fibre cutting angle of 118°–133° is in good agreement with previous

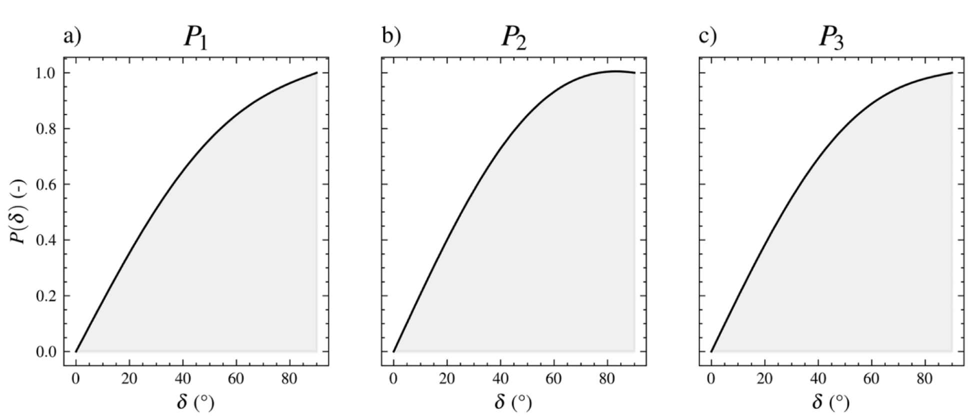

Fig. 13. $P(\theta'_c - \delta \leq \theta' \leq \theta'_c + \delta)$ probability functions determined based on the data of a) P_1, b) P_2 and c) P_3 projects.

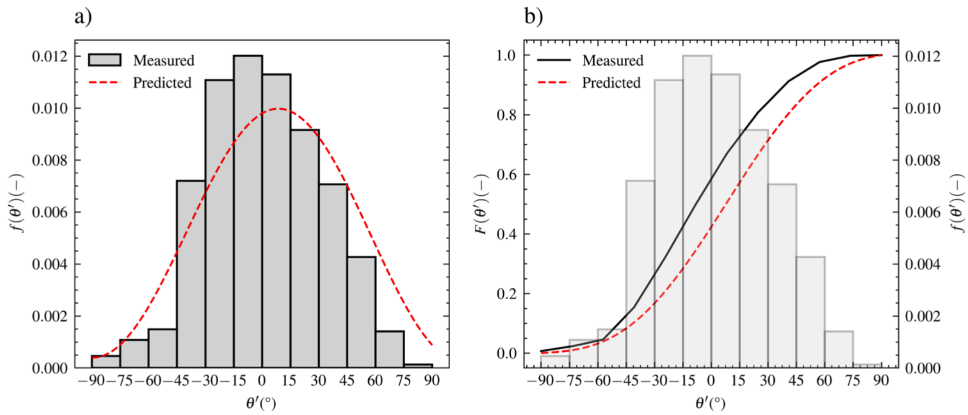

Fig. 14. Deviation of the mean of a) density functions and b) distribution functions fitted to the datasets of projects $P_{1–3}$ from the validation dataset.

findings. For instance, Wang et al. [39] identified 135° as the most burr-prone fibre cutting angle among those tested (0°, 45°, 90°, and 135°), and Li et al. [17] reported similar results. These consistent observations underscore the reliability of our angular predictions. Crucially, while earlier studies have focused solely on pinpointing the critical angle or defining a risky-angle range (Hrechuk et al. [24]), our work presents a closed-form trigonometric probability-density function for predicting burr-prone cutting angles in CFRP hole machining. This innovative model accurately represents the non-Gaussian distribution of burr occurrences over the entire 0°–180° spectrum, yet remains computationally efficient thanks to its simple analytical form.

The present study's findings support smart machining technology planning of non-unidirectional CFRPs (non-woven mat or chopped reinforced polymer composites). For example, the machining-induced burr can be accurately predicted if the CFRP plate surface is captured and the images are processed using conservative or machine learning algorithms to determine fibre directions relative to the hole contour [33]. Although the results are promising, they contain many limitations and constraints regarding their applicability. These main conditions – without claiming to be exhaustive – are the following: (i) the tool condition and the cutting technology is such that it results in a machining-induced burr on the edge contour of the hole (*e.g.* slightly worn tool, unfavourable support conditions, dry cutting, high feed); (ii) an excess of projected material observed on a ring characterized by circles corresponding to 0.97 and 0.93 times the nominal hole contour is considered as machining-induced burr; (iii) the reinforcing fibres are nominally unidirectionally arranged in the polymer matrix; (iv) the CFRP composite is sufficiently well impregnated and has adhesion to minimize the risk of interlayer burr formation; (v) the CFRP composite has a flat plate shape. In order to expand the applicability of the results and support industrial implementation, we recommend conducting further targeted tests in the future.

4. Conclusions

In the present study, we have developed models to predict the density and distribution of risky fibre cutting angles where machining-induced burr are formed in unidirectional carbon fibre reinforced polymer (UD-CFRP) composites. The coefficients of the models were determined using datasets of three previous research projects (*i.e.,* 2 380 808 data points), and validated through a fourth one (208 571 data points). According to the present study, the following main conclusions can be drawn:

- Statistical tests (Shapiro–Wilk and Kolmogorov–Smirnov) on over 2.38 million data points from three projects confirm that the angular distribution of burr occurrences deviates significantly from a normal distribution ($p \ll 0.05$).
- A fourth-order polynomial and a closed-form trigonometric function were fitted to the risky fibre cutting angle histograms. Both achieve excellent goodness-of-fit ($R^2 = 0.937–0.991$), but the trigonometric model—requiring only four coefficients—balances accuracy (minimum $R^2 = 0.949$) with very low computational cost, making it the preferred choice for real-time or embedded applications.
- Integrating the trigonometric density yields distribution functions with $R^2 \geq 0.997$ across all datasets, and a maximum absolute relative error below 3 % over the full 0°–180° range. This enables the reliable calculation of burr-formation probability within any specified angular window.
- Independent validation using a fourth dataset (208 571 points) confirms the predictive capability of our models, with $R^2 = 0.834$ for the density and $R^2 = 0.977$ for the distribution functions.
- The trigonometric model provides a ready-to-use tool for machining-process planning, allowing engineers to predict high-risk angular sectors around hole contours and adjust cutter paths or parameters accordingly. To facilitate industrial adoption, future studies should extend this framework to quantify how tool wear, lubrication, and cutting conditions shift the risky-angle distribution, adapt the models for multidirectional and woven CFRP laminates, including interlayer burrs in poorly bonded regions, and investigate burr formation on non-planar surfaces and large-diameter holes.

By capturing both the statistical nature of burr formation and providing a simple, closed-form solution, our work lays the groundwork for smarter, burr-aware machining strategies in CFRP manufacturing.

Declaration of generative AI and AI-assisted technologies in the writing process

During the preparation of this work the authors used ChatGPT in order to improve the English texting. After using this tool, the authors reviewed and edited the content as needed and take full responsibility for the content of the publication.

Code availability

Not applicable.

Ethics approval

Not applicable.

Consent to participate

Not applicable.

Consent for publication

Not applicable.

Funding

Not applicable.

CRediT authorship contribution statement

Norbert Geier: Writing – review & editing, Writing – original draft, Methodology, Investigation, Conceptualization. **Gergely Magyar:** Visualization, Software, Methodology, Formal analysis, Data curation.

Declaration of competing interest

The authors declare that they have no known competing financial interests or personal relationships that could have appeared to influence the work reported in this paper.

Acknowledgements

This research was partly supported by the János Bolyai Research Scholarship of the Hungarian Academy of Sciences No. BO/00508/22/6 and supported by the Doctoral Excellence Fellowship Programme (DCEP) is funded by the National Research Development and Innovation Fund of the Ministry of Culture and Innovation and the Budapest University of Technology and Economics, under a grant agreement with the National Research, Development and Innovation Office. The project has been partly implemented with the support provided by the Ministry of Culture and Innovation of Hungary from the National Research, Development and Innovation Fund, financed under the EKÖP-24-4-II-BME-157 and EKÖP-24-3-BME-383 funding scheme. The authors acknowledge the support of Norbert Ibriksz, György Póka, Dániel István Poór and Csongor Pereszlai in the experimental work.

Data availability

The data that support the findings of this study are available from the corresponding author, upon reasonable request.

References

[1] F. Wang, J. Deng, R. Fu, Y. Lin, Q. He, X. Ma, Dynamic modeling of thin-walled CFRP surface milling and the effect of chatter on surface quality, Int. J. Adv. Manuf. Technol. 132 (2024) 4765–4784, https://doi.org/10.1007/s00170-024-13612-w.

[2] T. Czigány, Special manufacturing and characteristics of basalt fiber reinforced hybrid polypropylene composites: mechanical properties and acoustic emission study, Compos. Sci. Technol. 66 (2006) 3210–3220, https://doi.org/10.1016/j.compscitech.2005.07.007.

[3] M. Perner, S. Algermissen, R. Keimer, H.P. Monner, Avoiding defects in manufacturing processes: a review for automated CFRP production, Robot Comput. Integr. Manuf. 38 (2016) 82–92, https://doi.org/10.1016/j.rcim.2015.10.008.

[4] W. Hintze, F. Brügmann, Influence of spatial tool inclination on delamination when milling CFRP, J. Mater. Process. Technol. 252 (2018) 830–837, https://doi.org/10.1016/j.jmatprotec.2017.10.041.

[5] M.R. Khosravani, K. Weinberg, Experimental investigations of the environmental effects on stability and integrity of composite sandwich T-joints, Materwiss Werksttech 48 (2017) 753–759, https://doi.org/10.1002/mawe.201600747.

[6] J. Ahmad, Machining of Polymer Composites, Springer US, 2009.

[7] J. Xu, T. Lin, J.P. Davim, M. Chen, M. El Mansori, Wear behavior of special tools in the drilling of CFRP composite laminates, Wear 476 (2021) 203738, https://doi.org/10.1016/j.wear.2021.203738.

[8] J. Xu, M. El Mansori, Wear characteristics of polycrystalline diamond tools in orthogonal cutting of CFRP/Ti stacks, Wear 376–377 (2017) 91–106, https://doi.org/10.1016/j.wear.2016.11.038.

[9] H. Wang, Z.J. Pei, W. Cong, A mechanistic cutting force model based on ductile and brittle fracture material removal modes for edge surface grinding of CFRP composites using rotary ultrasonic machining, Int. J. Mech. Sci. 176 (2020) 105551, https://doi.org/10.1016/j.ijmecsci.2020.105551.

[10] D. Geng, Y. Liu, Z. Shao, Z. Lu, J. Cai, X. Li, et al., Delamination formation, evaluation and suppression during drilling of composite laminates: a review, Compos. Struct. 216 (2019) 168–186, https://doi.org/10.1016/j.compstruct.2019.02.099.

[11] N. Geier, J. Paulo Davim, T. Szalay, Advanced cutting tools and technologies for drilling carbon fibre reinforced polymer (CFRP) composites: a review, Compos. Part A: Appl. Sci. Manuf. 125 (2019) 105552, https://doi.org/10.1016/j.compositesa.2019.105552.

[12] J.C. Aurich, D. Dornfeld, P.J. Arrazola, V. Franke, L. Leitz, S. Min, Burrs—Analysis, control and removal, CIRP Ann. 58 (2009) 519–542, https://doi.org/10.1016/j.cirp.2009.09.004.

[13] S. Ashworth, J.P.A. Fairclough, Y. Takikawa, R. Scaife, H. Ghadbeigi, K. Kerrigan, et al., Effects of machine stiffness and cutting tool design on the surface quality and flexural strength of edge trimmed carbon fibre reinforced polymers, Compos. Part A: Appl. Sci. Manuf. 119 (2019) 88–100, https://doi.org/10.1016/j.compositesa.2019.01.019.

[14] N. Geier, C. Pereszlai, Analysis of characteristics of surface roughness of machined CFRP composites, Period. Polytech. 64 (2020) 67–80, https://doi.org/10.3311/PPme.14436.

[15] A. Abdelhafeez Hassan, S.L. Soo, D.K. Aspinwall, D. Arnold, A. Dowson, An analytical model to predict interlayer burr size following drilling of CFRP-metallic stack assemblies, CIRP Ann. 69 (2020) 109–112, https://doi.org/10.1016/j.cirp.2020.04.038.

[16] B. Zhang, F. Wang, Q. Wang, X. Zhao, Novel fiber fracture criteria for revealing forming mechanisms of burrs and cracking at hole-exit in drilling Carbon Fiber Reinforced Plastic, J. Mater. Process. Technol. 289 (2021) 116934, https://doi.org/10.1016/j.jmatprotec.2020.116934.

[17] M. Li, M. Huang, X. Jiang, C. Kuo, X. Yang, Study on burr occurrence and surface integrity during slot milling of multidirectional and plain woven CFRPs, Int. J. Adv. Manuf. Technol. 97 (2018) 163–173, https://doi.org/10.1007/s00170-018-1937-6.

[18] N. Geier, T. Szalay, M. Takács, Analysis of thrust force and characteristics of uncut fibres at non-conventional oriented drilling of unidirectional carbon fibre-reinforced plastic (UD-CFRP) composite laminates, Int. J. Adv. Manuf. Technol. 100 (2018) 3139–3154, https://doi.org/10.1007/s00170-018-2895-8.

[19] F. Su, J. Yuan, F. Sun, Z. Wang, Z. Deng, Analytical cutting model for a single fiber to investigate the occurrences of the surface damages in milling of CFRP, Int. J. Adv. Manuf. Technol. 96 (2018) 2671–2685, https://doi.org/10.1007/s00170-018-1797-0.

[20] A.P. Jaiswal, H.W. Park, Experimental and analytical examination of multidirectional carbon fiber–reinforced polymers for uncut fibers and their distributions during drilling, Int. J. Adv. Manuf. Technol. 123 (2022) 1323–1339, https://doi.org/10.1007/s00170-022-10215-1.

[21] F. Su, Z. Deng, X. Qiu, F. Sun, Q. Wu, Morphological characteristics and formation mechanisms of the UD-CFRP drill exit-damages, Int. J. Adv. Manuf. Technol. 107 (2020) 2363–2374, https://doi.org/10.1007/s00170-020-05186-0.

[22] A.S. Shinde, I. Siva, Y. Munde, M.T. Hameed Sultan, L.S. Hua, F.S. Shahar, Numerical modelling of drilling of fiber reinforced polymer matrix composite: a review, J. Mater. Res. Technol. 20 (2022) 3561–3578, https://doi.org/10.1016/j.jmrt.2022.08.063.

[23] G. Bi, X. Wang, Y. Shi, C. Zhang, X. Zhao, Numerical investigation of the impact of processing conditions on burr formation in Carbon Fiber-Reinforced Plastic (CFRP) drilling with multiscale modeling, Mater. (Basel) 18 (2025) 1244, https://doi.org/10.3390/ma18061244.

[24] A. Hrechuk, V. Bushlya, J.-E. Ståhl, Hole-quality evaluation in drilling fiber-reinforced composites, Compos. Struct. 204 (2018) 378–387, https://doi.org/10.1016/j.compstruct.2018.07.105.

[25] J. Xu, Q. An, M. Chen, A comparative evaluation of polycrystalline diamond drills in drilling high-strength T800S/250F CFRP, Compos. Struct. 117 (2014) 71–82, https://doi.org/10.1016/j.compstruct.2014.06.034.

[26] J. Xu, C. Li, S. Mi, Q. An, M. Chen, Study of drilling-induced defects for CFRP composites using new criteria, Compos. Struct. 201 (2018) 1076–1087, https://doi.org/10.1016/j.compstruct.2018.06.051.

[27] Z. Jia, C. Zhang, F. Wang, R. Fu, C. Chen, An investigation of the effects of step drill geometry on drilling induced delamination and burr of Ti/CFRP stacks, Compos. Struct. 235 (2020) 111786, https://doi.org/10.1016/j.compstruct.2019.111786.

[28] N. Geier, G. Póka, T. Szalay, Direct monitoring of hole damage in carbon fibre-reinforced polymer (CFRP) composites, IOP Conf. Ser.: Mater. Sci. Eng. 448 (2018) 012003, https://doi.org/10.1088/1757-899X/448/1/012003.

[29] N. Geier, G. Póka, C. Pereszlai, Monitoring of orbital drilling process in CFRP based on digital image processing of characteristics of uncut fibres, Procedia CIRP 85 (2019) 16–170, https://doi.org/10.1016/j.procir.2019.09.011.

[30] N. Ibriksz, N. Geier, Analysis of uncut fibres at machined holes in carbon fibre-reinforced plastics (CFRP) using digital image processing, Bánki Rep. 1 (2018) 11–14.

[31] G. Magyar, D. Károly, J. Xu, N. Geier, Analysis of drilling-induced geometrical damages in basalt and carbon fibre-reinforced polymer (BFRP and CFRP) composites, Int. J. Adv. Manuf. Technol. (2022), https://doi.org/10.1007/s00170-022-10173-8.

[32] D. István Poór, N. Geier, C. Pereszlai, J. Xu, A critical review of the drilling of CFRP composites: burr formation, characterisation and challenges, Compos. B: Eng. (2021) 109155, https://doi.org/10.1016/j.compositesb.2021.109155.

[33] N. Geier, G. Póka, Á. Jacsó, C. Pereszlai, A method to predict drilling-induced burr occurrence in chopped carbon fibre reinforced polymer (CFRP) composites based on digital image processing, Compos. B: Eng. 242 (2022) 110054, https://doi.org/10.1016/j.compositesb.2022.110054.

[34] F. Lissek, J. Tegas, M. Kaufeld, Damage quantification for the machining of CFRP: an introduction about characteristic values considering shape and orientation of

drilling-induced delamination, Procedia Eng. 149 (2016) 2–16, https://doi.org/10.1016/j.proeng.2016.06.632.
[35] Perfortek Kft. n.d. https://www.perfortek.hu (accessed August 21, 2025).
[36] SD205A-11.138-53-12R1-C1 | Secotools.com n.d. https://www.secotools.com (accessed August 21, 2025).
[37] N. Otsu, A threshold selection method from gray-level histograms, IEEE Trans. Syst. Man. Cybern. 9 (1979) 62–66, https://doi.org/10.1109/TSMC.1979.4310076.
[38] G. Magyar, N. Geier, Analysis and modelling of thrust force in drilling of basalt and carbon fibre-reinforced polymer (BFRP and CFRP) composites, J. Braz. Soc. Mech. Sci. Eng. 45 (2023) 323, https://doi.org/10.1007/s40430-023-04241-7.
[39] F. Wang, J. Yin, J. Ma, Z. Jia, F. Yang, B. Niu, Effects of cutting edge radius and fiber cutting angle on the cutting-induced surface damage in machining of unidirectional CFRP composite laminates, Int. J. Adv. Manuf. Technol. 91 (2017) 3107–3120, https://doi.org/10.1007/s00170-017-0023-9.